Numerical investigation of water and temperature distributions in a proton exchange membrane electrolysis cell

WANG ZhiMing, XU Chao[*], WANG XueYe, LIAO ZhiRong & DU XiaoZe

Key Laboratory of Power Station Energy Transfer Conversion and System of MOE, School of Energy Power and Mechanical Engineering, North China Electric Power University, Beijing 102206, China

A three-dimensional, non-isothermal, two-phase model for a PEM water electrolysis cell (PEMEC) is established in this study. An effective connection between two-phase transport and performance in the PEMECs is built through coupling the liquid water saturation and temperature in the charge conservation equation. The distributions of liquid water and temperature with different operating (voltage, temperature, inlet velocity) and physical (contact angle, and porosity of anode gas diffusion layer) parameters are examined and discussed in detail. The results show that the water and temperature distributions, which are affected by the operating and physical parameters, have a combined effect on the cell performance. The effects of various parameters on the PEMEC are of interaction and restricted mutually. As the voltage increases, the priority factor caused by the change of inlet water velocity changes from the liquid water saturation increase to the temperature drop in the anode catalyst layer. While the priority influence factor caused by the contact angle and porosity of anode gas diffusion layer is the liquid water saturation. Decreasing the contact angle or/and increasing the porosity can improve the PEMEC performance especially at the high voltage. The results can provide a better understanding of the effect of heat and mass transfer and the foundation for optimization design.

proton exchange membrane electrolysis cell, two-phase model, liquid water saturation, flow rate, temperature distribution

1   Introduction

In recent years, hydrogen has attracted considerable attention and gained widespread use [1,2], because of its high calorific value, environmentally friendly and flexible energy storage capability. Hydrogen can be produced from various sources such as fossil fuels via steam reforming/gasification, biomass via pyrolysis/gasification, and water via electrolysis/thermolysis/photolysis [3]. Among the aforementioned techniques, the proton exchange membrane (PEM) water electrolysis driven by renewable energy sources is regarded as a promising candidate to reduce carbon emissions and environmental pollution due to its outstanding ability for hydrogen production with increased energy efficiency and specific production capacity [4].

In the past decades, considerable research work has been made to investigate critical issues associated with performance, durability and cost of PEM electrolysis cells (PEMECs) [5]. Some experiments about the influence of structure and flow behaviour on the performance of PEMEC have been carried out. Ito et al. [6] studied three different types of flow fields (serpentine-single, serpentine-dual, and parallel), and investigated the influence of fluid flow characteristics on the cell performance and pressure drop. The

results showed that there was an intimate relationship between flow regime and cell performance, especially in the slug and annular regime. They further investigated the effect of different porosities and pore diameters of current collectors [7]. It was found that bubbles could restrict the mass transport of liquid water to the electrode surface and the membrane, and little pore diameter could restrain the generation of larger bubbles, thus improving the electrolysis performance. Many advanced methods, such as high-speed imaging [8], optical visualization [9] and neutron radiography with optical imaging [10], were used to investigate the gas-liquid flow in the PEMEC. Majasan et al. [11] studied the two-phase flow behaviour in both the single serpentine flow field and the parallel flow field using the high-speed optical imaging. Although water flow rate influenced the length of bubbles and gas slugs, it was observed that its effect on cell performance depended strongly on the operating temperature. Lee et al. [12] investigated the temperature-dependent gas saturation via in *operando* neutron imaging of a PEMEC. The reduction of gas saturation in the porous transport layer (PTL) and the promotion of uniform gas distributions near the catalyst layer (CL)-PTL interface were observed with the increase of operating temperature at the same current density.

Numerical investigations have been carried out in order to further study the effects of operating and physical parameters on the performance of PEMECs. One-dimensional (1-D) models of PEMEC have been built to predict the general behavior [13], to study the effect of different parameters [14,15], or to explore the control strategies [16]. Since 1-D models can not estimate proton and mass transport in PEMECs, more complicated models have been established to improve the understanding of two-phase flow and flow field design. Grigoriev et al. [17] reported a two-phase mathematical model to analyze the performance of PEMEC with different geometrical and operating parameters. Han et al. [18] developed a two-phase mathematical model and discussed the influences of the contact angle, porosity and thickness of liquid/gas diffusion layer (LGDL). Aubras et al. [19] developed a 2-D model to investigate the water management. The results showed that the bubble coalescence phenomenon had influence on mass transfer, ohmic resistance and the efficiency. Kaya et al. [20] developed a 2-D model to compare Pt and Pt/Ir anodic catalysts and to determine the operating parameters for different PEMECs. They found that a higher temperature increased the cell performance because of easy transport of species, higher exchange of current density and conductivity. Zinser et al. [21] developed a spatially distributed model which can predict stationary saturation profiles and detect drying-out behaviour at the anodic CL. However, due to the limitations of the 2-D model, the effect of rib on the non-uniform mass and heat transport cannot be observed. Moreover, most researchers mainly focused on the two-phase transport behavior in the PTL.

Nie et al. [22] performed a 3-D numerical simulation of parallel anode flow field to examine the pressure and velocity distributions. Then Nie and Chen [23] conducted a two-phase, 3-D numerical model to investigate distributions of flow velocity, pressure and volume fraction of products in the flow field of the anode. De Haro Ruiz et al. [24] performed a 3-D numerical analysis for a high temperature PEM electrolyzer to investigate three designs of the channel structure, namely parallel, multi-path serpentine, and single serpentine. Among the tested designs, the multi-serpentine type showed better performance in terms of hydrogen production and uniformity of temperature and pressure drop. Olesen et al. [25] developed a two-phase flow model in which heat transfer as well as turbulence was taken into account for studying the gas-liquid flow within channels and PTL. The model was supplemented and improved by incorporating electrochemistry as well as detailed heat and two-phase flow transport phenomena in ref. [26]. Lafmejani et al. [27] developed a 3-D, VOF model to study the gas-liquid flow in the channel and PTL in an interdigitated flow field. The oscillating transition from slug, plug and bubble flow in the outgoing channels could be obtained and had impact on the distribution of liquid water within the PTL. Toghyani et al. [28] investigated the cell performance with five different flow fields using a 3-D CFD simulation. The results showed that the two-path serpentine flow pattern provided uniform distribution of current density, temperature and hydrogen fraction. Upadhyay et al. [29] developed a transient, 3-D single phase model to investigate six different inlet and outlet configurations. It was found that the average pressure drop decreased with the increase of inlet number. Zhang et al. [30] established a full-scale, two-phase, single-channel model and calculated two cases with the bipolar plates or not. Effective water and thermal management strategies were proposed based on the numerical results. Moreover, a wealth of newly-built AI-related research methods have been proposed in many energy fields, such as energy utilization, energy conversion and energy materials [31]. Wang et al. [32] used a deep learning method based on a convolutional neural network (CNN) to predict the effective diffusivity of a porous medium. Compared with LBM, the CNN with a strong learning ability achieved a low relative error in the prediction with porosities ranging from 0.39 to 0.79. It would be an exciting thing if further models are extended to the whole PEMEC and stack, but there is still a long way to go.

From the above review, most simulation work focused on the two-phase transport behavior in the PTL by using a 2-D two-phase model or the performance with different structures using a 3-D single phase model. However, effective connection between two-phase transport and performance in

the PEMECs is not established. It is crucial to gain more insights about the relation between two-phase transport, heat transport and electrolysis performance of PEMECs based on a 3-D structure, especially at high current densities. To this end, this study aims to build a 3-D, non-isothermal, two-phase model and explore the behavior of mass and heat distributions inside the PEMECs. Furthermore, the comprehensive effects of operating parameters (voltage, inlet temperature and inlet velocity) and physical parameters (AGDL porosity and contact angle) are addressed in detail. The results can provide a better understanding of the effect of heat and mass transfer on the electrolysis performance and the foundation for the optimization design.

2   Physical and numerical model

2.1   Physical model

Figure 1(a) presents the 3-D module of a typical PEMEC with parallel channels in both the anode and cathode sides. Because of the symmetric structure, the module includes half of the anode bipolar plate (ABP), half of the cathode bipolar plate (CBP), half of the anode flow channel (ACH), half of the cathode flow channel (CCH), the gas diffusion layers (AGDL and CGDL) in the anode and cathode, the catalyst layers (ACL and CCL) in the anode and cathode, and the proton exchange membrane (PEM).

Table 1 lists the geometrical parameters of the physical module for the PEMEC. During operation, water flows through the ACH where some water diffuses across the AGDL to the ACL. Then those water is split into protons, electrons and oxygen, as shown in eq. (1). The produced protons pass through the PEM to the CCL under the effect of electric field force, and react with the electrons which come from the external circuit, as shown in eq. (2). In the cathode side, a water flow is also introduced into the CCH, since it can enhance the hydrogen evacuation and prevent the membrane drying, especially at high current densities [33].

$$H_2O \rightarrow 2H^+ + \frac{1}{2}O_2 + 2e^- \ (\text{Anode}) \tag{1}$$

$$2H^+ + 2e^- \rightarrow H_2 \ (\text{Cathode}) \tag{2}$$
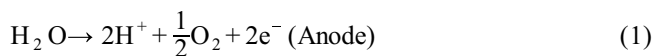
2.2   Numerical model

The working of PEMEC involves complex multiphysics processes, such as the transport of charge, liquid water, gas and heat. To solve the above mentioned physical problem, the numerical model is established based on the conservation equations of mass, charge, momentum and energy to investigate the influence of liquid water and temperature distribution on the performance of PEMEC. The following assumptions are adopted to develop the numerical model:

(1) The evaporation of liquid water is neglected [19] because water mainly exist in liquid form;

(2) The gas phase is considered as an incompressible ideal gas [34];

(3) The diffusions of hydrogen and oxygen through the membrane are negligible because the amount is exceedingly small;

(4) The flow in the ACH and CCH is laminar because of small Reynolds number;

(5) The contact resistances between all the adjacent components are neglected [35];

(6) The AGDL, CGDL, ACL and CCL are isotropic and homogenous [30].

2.2.1   Charge transport and conservation

Considering the chemical reaction is affected by the concentrations of reactants and the local temperature, the Butler-Volmer equation is modified to be the following formulas (eqs. (3) and (4)) for the anode and cathode, respectively [18,26]. Since the exchange current density is affected even more in the anode, $i_{0,a}e^{\left(-\frac{E_{exc}}{R}\left(\frac{1}{T}-\frac{1}{353.15}\right)\right)}$ is used to modify the equation [20,36]:

$$i_{v,a} = sa_{v,a}i_{0,a}e^{\left(-\frac{E_{exc}}{R}\left(\frac{1}{T}-\frac{1}{353.15}\right)\right)}$$
$$\left(\exp\left(\frac{\alpha_a F\eta}{RT}\right) - \exp\left(\frac{-\alpha_c F\eta}{RT}\right)\right), \tag{3}$$

$$i_{v,c} = sa_{v,c}i_{0,c}\left(\exp\left(\frac{\alpha_a F\eta}{RT}\right) - \exp\left(\frac{-\alpha_c F\eta}{RT}\right)\right), \tag{4}$$

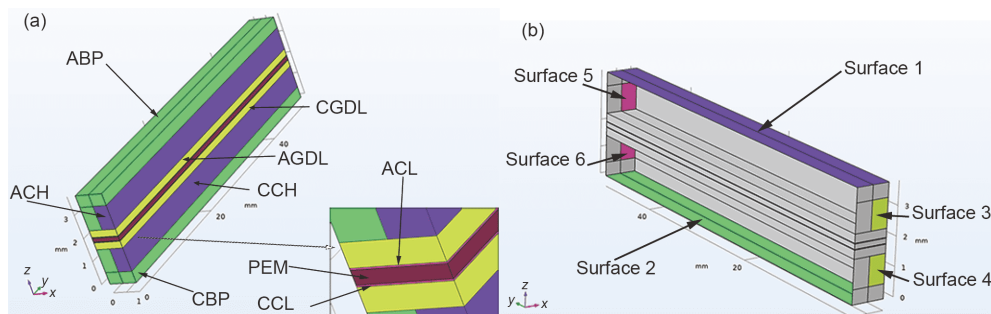where subscripts a and c represent the anode and cathode,

Figure 1   (Color online) Computational domain of the PEMEC module. (a) Structure composition; (b) boundary.

Table 1 Geometrical parameters of the PEMEC module

Parameter	Value
Channel length (mm)	50
Channel width (mm)	0.5
Channel height (mm)	1
Bipolar plate height (mm)	1.5
Rib width (mm)	0.5
GDL thickness (μm)	300
Catalyst thickness (μm)	20
Membrane thickness (μm)	178

respectively. a_v, i_0 and α are the specific active surface area, the reference exchange current density and the charge transfer coefficient, respectively. F and R indicate the Faraday constant and gas constant, respectively. T represents the temperature. E_{exc} is the activation energy for the electrode reactions, and is assumed as 53.99 kJ/mol [20]. The activation overpotential η is defined as the difference between the electronic and ionic potentials:

$$\eta = \varphi_s - \varphi_m - E_{eq}. \tag{5}$$

The equilibrium voltage E_{eq} is equal to zero on the cathode and can be calculated by the following equation on the anode:

$$E_{eq} = 1.229 - 9.0 \times 10^{-4}(T - 298.15). \tag{6}$$

The charge balance equations for electrons and protons can be described on the basis of the generalized Ohm's law, respectively:

$$\nabla \cdot (-\sigma_s \nabla \varphi_s) = S_{\varphi,s}, \tag{7}$$

$$\nabla \cdot (-\sigma_m \nabla \varphi_m) = S_{\varphi,m}, \tag{8}$$

where subscripts s and m represent the electronic and ionic charges, respectively. S_φ denotes a general source term which is related to the reaction rates of electrons and protons. σ is the conductivity, and σ_m can be written as a function of water content and temperature:

$$\sigma_m = (0.5139\lambda - 0.326)\exp\left[1268\left(\frac{1}{303} - \frac{1}{T}\right)\right], \tag{9}$$

where λ is the water content of the membrane [37]. The membrane can be considered to be fully saturated with liquid water, and thus λ is assumed to 16 in the present model [38].

2.2.2 Transport of liquid water
The continuity equation is used to calculate the mass conservation of liquid water in the CHs, GDLs and CLs of anode and cathode:

$$\nabla \cdot (\rho_l \mathbf{u}_l) = S_m, \tag{10}$$

where ρ_l is the density of water. $\mathbf{u}_l$ indicates the velocity of water. S_m refers to the mass source term, which is caused by the consumption of water on the CLs.

The flow channel is assumed to be porous with a small width-length ratio (this study: 1/50), and the corresponding permeability is calculated by $K_{0,ACH}=1.227d^2/32$ [39], where d is the hydraulic diameter.

The momentum equation is

$$\frac{\rho_l}{\varepsilon^{eff}}(\mathbf{u}_l \cdot \nabla)\frac{\mathbf{u}_l}{\varepsilon^{eff}}$$
$$= \nabla \cdot \left[-p_l \mathbf{I} + \frac{\mu_l}{\varepsilon^{eff}}\left(\nabla \mathbf{u}_l + (\nabla \mathbf{u}_l)^T\right) - \frac{2}{3}\frac{\mu_l}{\varepsilon^{eff}}(\nabla \cdot \mathbf{u}_l)\mathbf{I}\right]$$
$$- \left(\frac{\mu_l}{K_0 K_{rl}} + \frac{S_m}{(\varepsilon^{eff})^2}\right)\mathbf{u}_l, \tag{11}$$

where p_l is the liquid water pressure, μ_l is the dynamic viscosity of liquid water, ε^{eff} represents the effective porosity which can be calculated through the intrinsic porosity of porous layers (ε): $\varepsilon^{eff} = \varepsilon \cdot s$, $\mathbf{I}$ is the mathematical symbol for transposition, and K_0 and K_{rl} are the absolute permeability and the relative permeability, respectively. K_{rl} is equal to the cube of liquid water saturation, $K_{rl} = s^3$.

2.2.3 Transport of gas phase
The continuity equation of gas phase is used in the CHs, GDLs and CLs of anode and cathode:

$$\nabla \cdot (\rho_g \mathbf{u}_g) = S_g, \tag{12}$$

where ρ_g is the density of gas. $\mathbf{u}_g$ indicates the velocity of gas. S_g refers to the mass source term, which is caused by the generation of gas on the CLs.

The capillary pressure for the porous region is given by [40]

$$p_c = p_g - p_l = \sigma\cos\theta\left(\frac{\varepsilon}{K_0}\right)^{0.5} J(s), \tag{13}$$

where σ is the surface tension for liquid water-air system, $J(s)$ represents the widely-used Leverette function:

$$J(s) = \begin{cases} 1.417(1-s) - 2.120(1-s)^2 + 1.263(1-s)^3, \\ 0° < \theta \leq 90°, \\ 1.417s - 2.120s^2 + 1.263s^3, \\ 90° < \theta \leq 180°. \end{cases} \tag{14}$$

p_g can be calculated in accordance with the Darcy's law for gas phase as

$$-\nabla p_g = \frac{\mu_g}{K_0 K_{rg}}\mathbf{u}_g. \tag{15}$$

By rearranging eqs. (10) and (12)–(15), conservation equation for liquid water saturation can be rewritten as [41]

$$\nabla \cdot \left(-\rho_g D_c \nabla s + \rho_g \frac{K_{rg}\mu_l}{K_{rl}\mu_g}\mathbf{u}_l\right) = S_g, \tag{16}$$

where D_c is the capillary diffusion coefficient and is expressed as

$$D_c = \frac{\sigma\cos\theta}{\mu_g}K_{rg}(\varepsilon K_0)^{1/2}\frac{dJ(s)}{ds}. \tag{17}$$

The energy equation for the entire computational domain can be described as

$$\nabla\left(\rho_{\mathrm{eff}} C_{\mathrm{p,eff}} \mathbf{u} T\right) = \nabla \cdot \left(k_{\mathrm{eff}} T\right) + S_T, \tag{18}$$

where ρ_{eff}, k_{eff} and $C_{\mathrm{p,eff}}$ are the effective density, the effective thermal conductivity and the specific heat capacity, respectively. S_T is the energy source term, which includes the irreversible heat, the entropy heat source and the ohmic heat source. The compounded density, specific heat capacity and conductivity are considered in accordance with the empirical equations:

$$\rho_{\mathrm{eff}} = (1-\varepsilon)\rho_{\mathrm{sa}} + \varepsilon\rho_{\mathrm{fm}}, \tag{19}$$

$$k_{\mathrm{eff}} = (1-\varepsilon)k_{\mathrm{sa}} + \varepsilon k_{\mathrm{fm}}, \tag{20}$$

$$C_{\mathrm{p,eff}} = (1-\varepsilon)C_{\mathrm{p,sa}} + \varepsilon C_{\mathrm{p,fm}}, \tag{21}$$

where subscripts sa and fm represent the solid areas and fluid mixture, respectively. The parameter values in the present model and the source terms for each sub-domain are summarized in the Tables S1 and S2 of Supporting Information , respectively.

2.3 Boundary conditions

The main boundaries and conditions for each conservation equation are shown in Figure 1(b) and Table S3 of the Supporting Information, respectively. The fluid flows into the cell from surface 3 and 4 with constant inlet temperature and velocity, and then exits from surface 5 and 6 with con-

stant pressure. The thermal insulated surface 1 and 2 are set as the potential and electric ground, respectively. The left and right sides of the model are the symmetrical construction, and the other impervious surfaces are set as electrical and thermal insulation boundary conditions.

3 Numerical procedure and model validation

In this work, the numerical model is built in the commercial software COMSOL Multiphysics on a eighteen-core 3.0 GHz Dell workstation with 128 GB RAM. The Secondary Current Distribution module, Free Flow in Porous Media module, Heat transfer module and Classical PDE are selected to solve the charge transfer, conservation of mass and momentum, heat transfer and gas transport, respectively. Segregated method and Direct method on the basis of PARDISO solvers are used to solve each variable. The whole calculating domain divided into many rectangles which is shown in Figure 2(a) is discretized by the finite element method (FEM). The convergence criteria is 1×10^{-5} for each variable. Figure 2(b) compares the calculated current densities with different element numbers when the voltage is 1.8 V. It can be seen that the grid with 203400 elements is fine enough for the present calculation.

To verify the numerical model, the present model is first used to calculate the polarization performance of a PEMEC based on the experimental conditions which were experi-
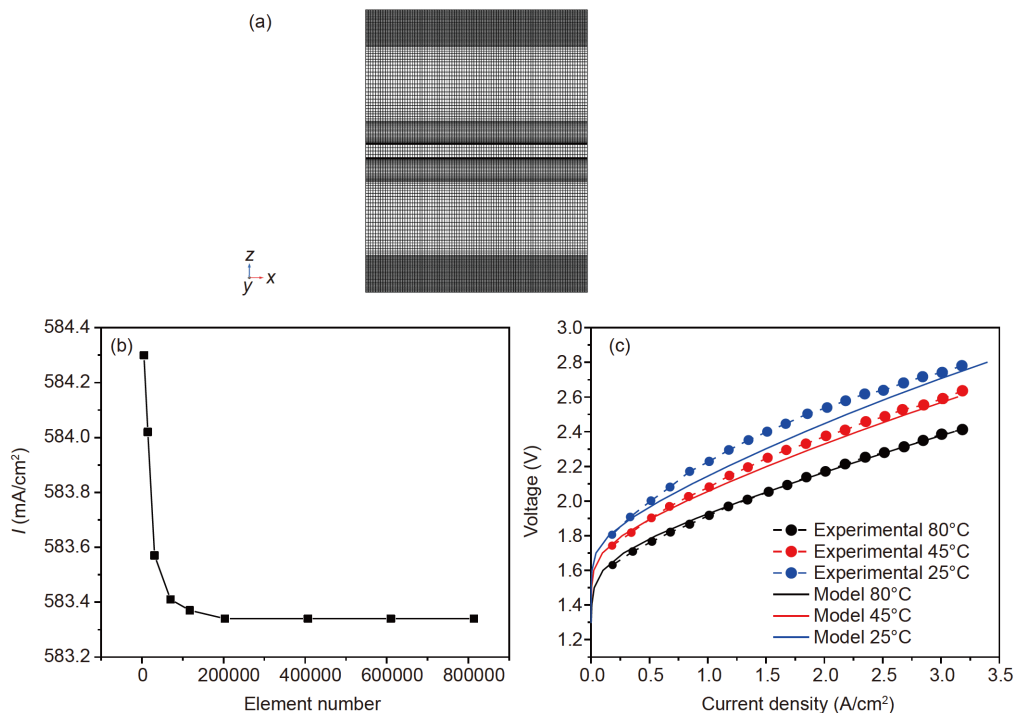
Figure 2 (Color online) (a) Grid map of *y*-axis cross section, (b) grid independence test and (c) comparison of numerical results and experimental data in different temperature.

mentally tested in ref. [11]. Figure 2(c) compares the polarization curves between the experimental data and the predicted results for the electrolyzer at different temperatures. It is clear that the numerical results are in good agreement with the experimental data for all the temperatures, indicating that the present model is credible to predict the performance of a PEMEC.

4   Results and discussion

Based on the above established model, the 3-D distributions of water and temperature can be obtained. The general behavior of water and temperature distributions is discussed firstly, and the influence of voltage on the water and temperature distributions is investigated. Then, the temperature and liquid water saturation in the ACL, which can directly affect the performance of PEMEC, are investigated with the changes of inlet temperature, inlet velocity, contact angle and AGDL porosity.

4.1   General behavior

In order to have a more intuitive understanding of the liquid water saturation and temperature distributions, the 3-D images are presented at the following conditions: the voltage is 2.0 V, inlet temperature is 80°C and inlet velocity of anode and cathode is 0.15 m/s (except for the studied parameters, other parameters are unchanged in the following parts).
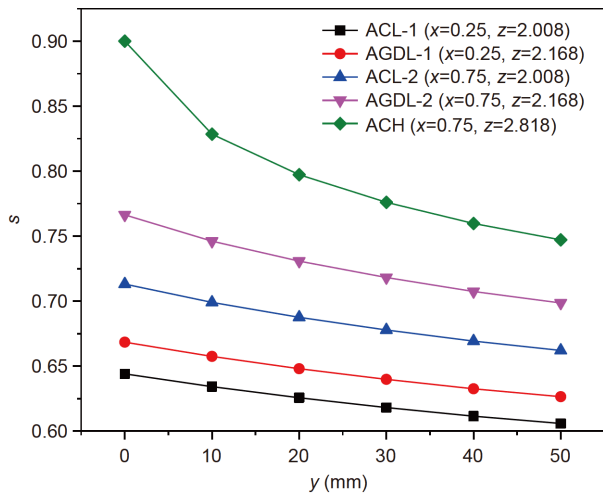
Figure 3 shows the distributions of liquid water saturation and the concentrations of oxygen and hydrogen. The cross-sections are at $x=1$ mm, $y=0, 10, 20, 30, 40, 50$ mm and $z=1.998$ mm (on the membrane-ACL interface), respectively. From Figure 3(a) and (b), it can be seen that the liquid water saturation decreases along the y-direction while increases along the x-direction. Along the z-direction, the liquid water saturation decreases from the channel to the CL for both the anode and cathode. From Figure 3(c) and (d), the tendencies of gas molar concentration in the anode and cathode are contrary to the tendencies of liquid water saturation. The above distributions are mainly caused by the fact that the chemical reaction takes place in the CLs. In the anode ACL, water is consumed and oxygen is generated. The gas oxygen diffuses into the ACH through the AGDL and is swept off by the water flow. As thus, the gas gradually converges along the flow direction in the ACH, resulting in the decrease of liquid water saturation. Similarly, hydrogen is generated in the CCL, and the gas hydrogen diffuses into the CCH through the CGDL and is carried away by water. Meanwhile, because of more difficult removal of gas bubbles from the porous region under the rib, the liquid water saturations in CLs under the rib are smaller than that facing the channel. The minimum values of liquid water saturation are 0.59 and 0.64 in the anode and cathode, respectively. Although the amount of hydrogen produced in the cathode is more than the amount of oxygen produced in the anode, the concentration distribution and magnitudes of oxygen and hydrogen have little difference. That is because gas bubbles could be swept
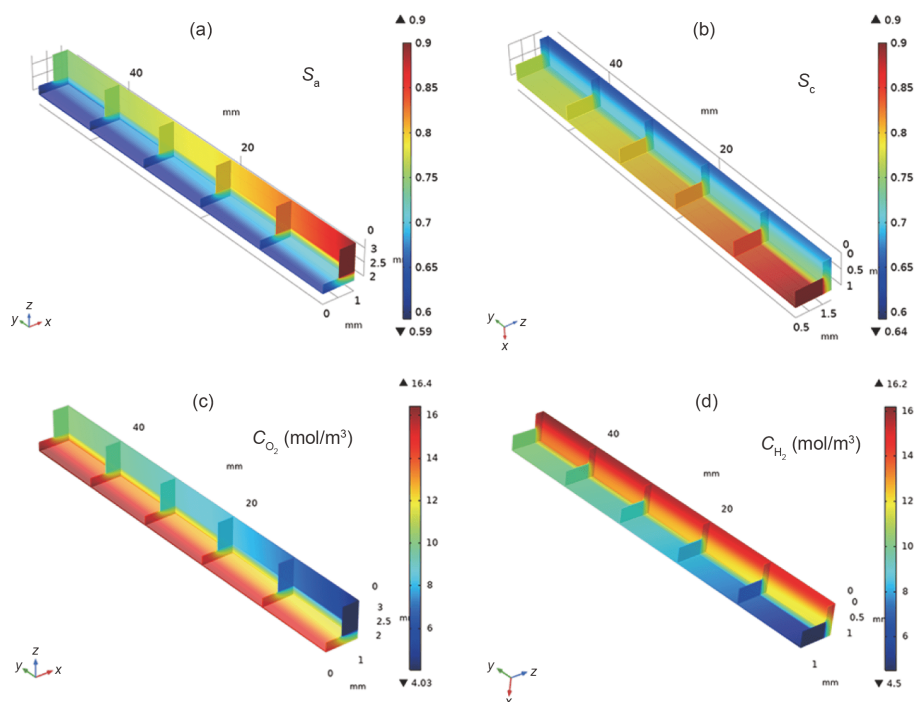
Figure 3   (Color online) The distributions of liquid water saturation in the anode (a) and cathode (b), and the molar concentrations of oxygen in the anode (c) and hydrogen in the cathode (d).

off quickly by the water flow.

The distributions of liquid water saturation along five typical lines are given in Figure 4 to further analyze the behavior of water distribution. The dots are the intersection of the six parallel cross-sections shown in Figure 3 and the five lines. Specifically, the five lines are the center of ACL under ABP (ACL-1), AGDL under ABP (AGDL-1), ACL under ACH (ACL-2), AGDL under ACH (AGDL-2) and ACH, respectively. It can be seen that the liquid water saturation decreases along the *y*-direction and the decreased values of liquid water saturation in AGDL and ACL are less than that in ACH. For example, the value of liquid water saturation in ACH falls from 0.9 to 0.75, while the value in ACL drops from 0.71 to 0.66. The combined effect of the increased oxygen and the decreased water flow in the ACH along the flow direction results in the greatest decrease of liquid water saturation in the channel. However, the drop of liquid water in ACL means that more serious mass transfer problem may occur downstream. The liquid water saturations of AGDL and ACL under ABP are significantly smaller than that under ACH. For example, the values of all dots on the black line are about 0.062 less than that on the blue line. It indicates that the
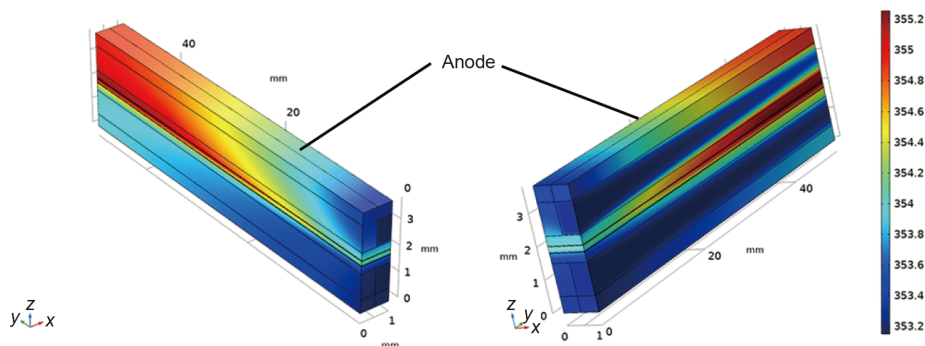
oxygen is more difficult to be removed from the small space under the ABP, which may cause more serious loss of mass-transfer polarization. Because of concentration gradient, the oxygen can diffuse from the ACL to the ACH. However, the oxygen under the rib requires a longer way to diffuse to the ACH than the oxygen in the ACL facing the channel.

Figure 5 shows the 3-D diagram of temperature distribution viewed from the left and right sides. Firstly, it can be seen that the temperature increases along the *y*-direction. When the cell is in operation, the conductive solid materials produce ohmic heat which is greater than the heat required for the reaction, resulting in the increase of cell temperature. Water is both a reactant and a coolant, but the decrease of liquid water saturation and the increase of the fluid temperature along the *y*-axis cause the drop of heat transfer performance. Secondly, the cathode temperature is lower than the anode temperature. This could be caused by the fact that heat is more easily taken away from the cathode side because of higher heat transfer performance of hydrogen than oxygen, no water consumption and higher velocity. Ultimately, there are two apparent temperature gradients along the flow direction and *z* direction.

The heat distribution under different voltages is studied, as shown in Figure 6. All dots represent the volume average temperature of ACL, AGDL, ABP and the fluid in ACH. It can be found that the temperature of all parts has little change when the voltage ranges from 1.3 to 1.6 V. Then each part of the PEMEC, especially the ACL, presents an exponential increase in the temperature with the increase of voltage from 1.6 to 2.4 V. The reason is that for a given PEMEC, according to the Ohm's law, the current increases with the increase of voltage, leading to higher ohmic heat, especially at the part of PEM which is the largest contributor to the ohmic resistance. Then heat is transferred successively to the ACL, AGDL, ABP and the water in the ACH. Because water flows into and out of the PEMEC and takes away heat continuously, the temperature of ACH is the lowest. Besides, the temperature difference within the PEMEC increases evidently with the increase of voltage. The temperature difference can reach to 3.7°C at the voltage of 2.4 V. Con-

Figure 4   (Color online) Distributions of liquid water saturation along the five lines (Lines 1–5) parallel to the *y*-axis.

**Figure 5**   (Color online) The temperature contours of the outside surfaces of the computational domain.
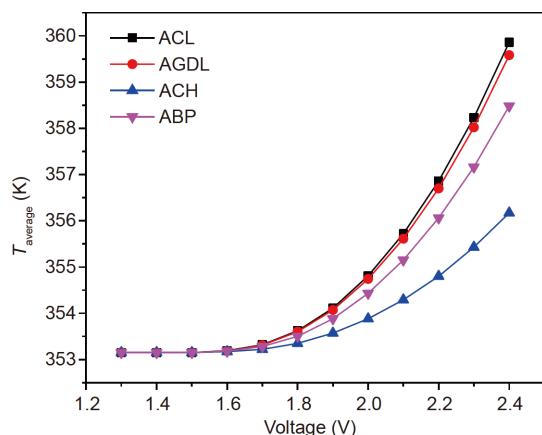
Figure 6 (Color online) The averaged temperature of different parts under different voltages with an inlet temperature of 80°C.

Figure 7 (Color online) The averaged liquid water saturations of different parts under different voltages.

sidering the temperature distribution shown in Figure 5, it can be concluded that the higher is the voltage, the more likely it is to cause the overheat at the end of the cell.

Figure 7 shows the volume averaged values of liquid water saturation in ACL, AGDL and ACH under different voltages. Firstly, the value of liquid water saturation decreases with the increased voltage. That is because as the voltage goes up, the current increases, and then more gas is produced in the PEMEC. The bubbles will cover the active sites of the catalyst and limit the water access [42], resulting in that a certain current density requires a higher voltage. Secondly, it can be seen that the liquid water saturation at the same voltage is in the order of $s_{ACH} > s_{AGDL} > s_{ACL}$, and the liquid water saturation in ACL decreases sharply from 0.83 to 0.54 with the increase of voltage from 1.6 to 2.4 V. This is because the chemical reaction takes place in the ACL, resulting in water consumption and oxygen generation, and the reaction rate is increased with the increase of voltage. This finding indicates that enhancing the oxygen bubbles removal from the ACL can improve the PEMEC performance, which has been proved in ref. [43].

4.2 Influences of inlet water temperature and inlet water velocity

The inlet water temperature is an important factor for the PEMEC performance, and the changes of water saturation in the ACL and current density under different inlet water temperature conditions is shown in Figure 8. Within the tested temperature range of 25°C to 80°C, increasing the temperature results in an evident improvement of the current density at each voltage. The well-known reason is that the water electrolysis is an endothermic reaction, and thus the reaction is promoted and the polarization loss is reduced with the temperature increase. Resulting from the increased current density, the liquid water saturation in the ACL is decreased with the inlet temperature increase, as shown in
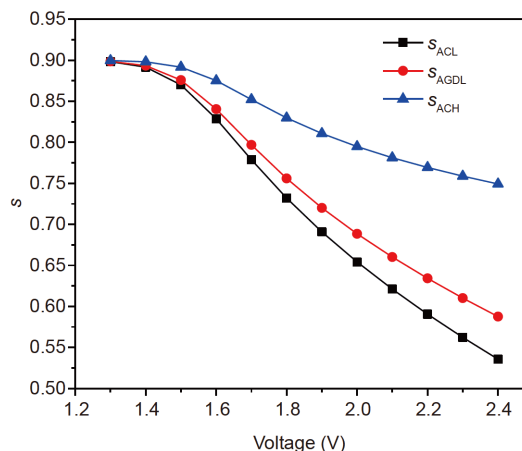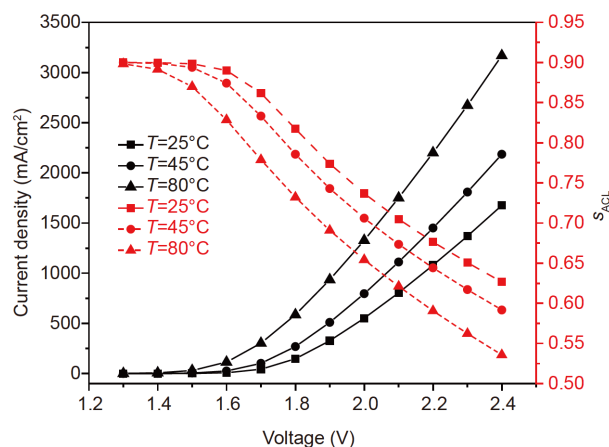

Figure 8 (Color online) The changes of the averaged water saturation of ACL and current density with different voltage under different inlet temperature conditions.

Figure 8. For example, when the voltage is 2.4 V, the current density increases from 1677 to 3168 mA/cm^2 and the liquid water saturation decreases from 0.63 to 0.54.

Although high temperature is benefit to the cell performance from above, local hot spot because of uneven distribution of temperature can accelerate the membrane degradation and cause higher gas cross-over [38]. Therefore, it is commonly adopted that the cell operating temperature is kept even lower (60°C–70°C) due to stability issues with ion-exchange resins used to maintain the purity of the process water [44].

The effect of the inlet velocity on the liquid water saturation in ACL, averaged temperature of ACL and current density is shown in Figure 9. It can be seen from Figure 9(a) that the liquid water saturation increases slightly when the inlet velocity increases from 0.3 to 1 m/s in the anode. That is because the increase of inlet velocity accelerates the gas removal from the ACH, also facilitating the gas removal from the AGDL and ACL. As for the averaged temperature
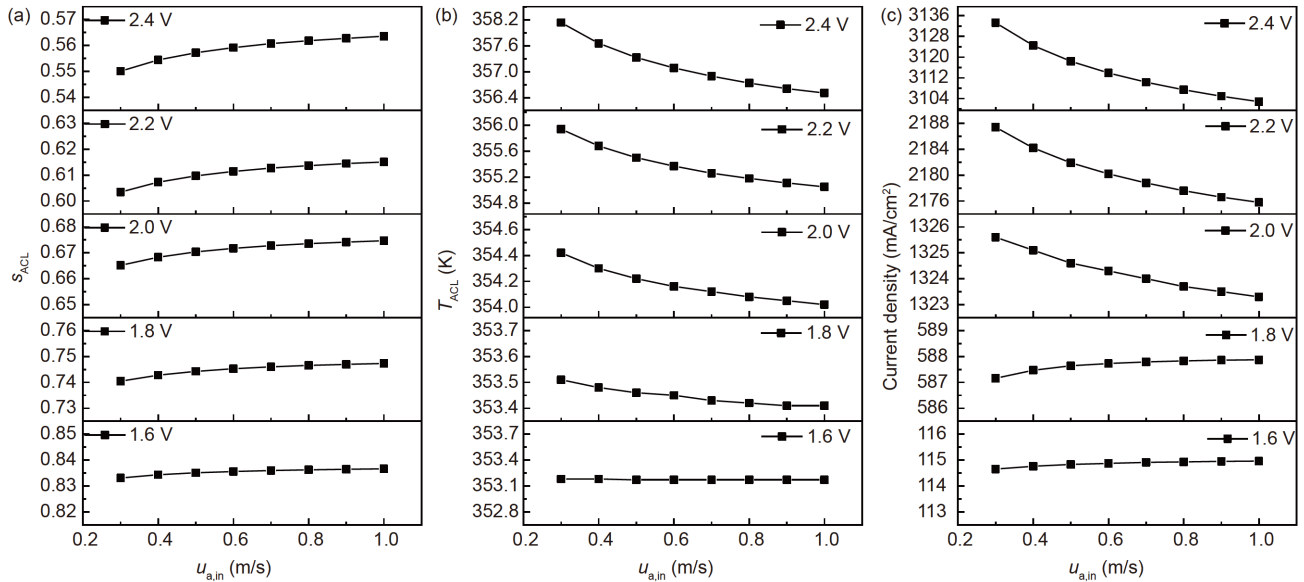
Figure 9   Variations of the liquid saturation in ACL (a), the averaged temperature of ACL (b), and the current density (c) with the inlet velocity at different voltages.

of ACL, it can be evidently reduced with the increase of the inlet velocity, especially at higher voltages. For example, the temperature decreases from 358.1 to 356.5 K at the voltage of 2.4 V. This is because the heat removal from the PEMEC can be quickened by the increase of inlet velocity.

The changes of liquid saturation and temperature of ACL can influence the current density, as shown in Figure 9(c). As the inlet velocity increases, the current density increases slightly when the voltage is below 1.8 V, while it decreases slightly when the voltage is higher than 2.0 V. This is caused by the trade-off of the increase of water saturation and decrease of temperature with the increase of inlet velocity. As

the voltage increases, the priority factor caused by the change of inlet water velocity changes from the liquid water saturation increase to the temperature drop in the ACL.

4.3   Influences of contact angle and porosity of AGDL

In this section, the effects of the contact angle and porosity of AGDL on the liquid saturation and temperature distributions in the ACL are investigated. Figure 10 presents the variations of liquid water saturation, averaged temperature and current density with the contact angle. It can be seen that the liquid water saturation in the ACL decreases evidently with the
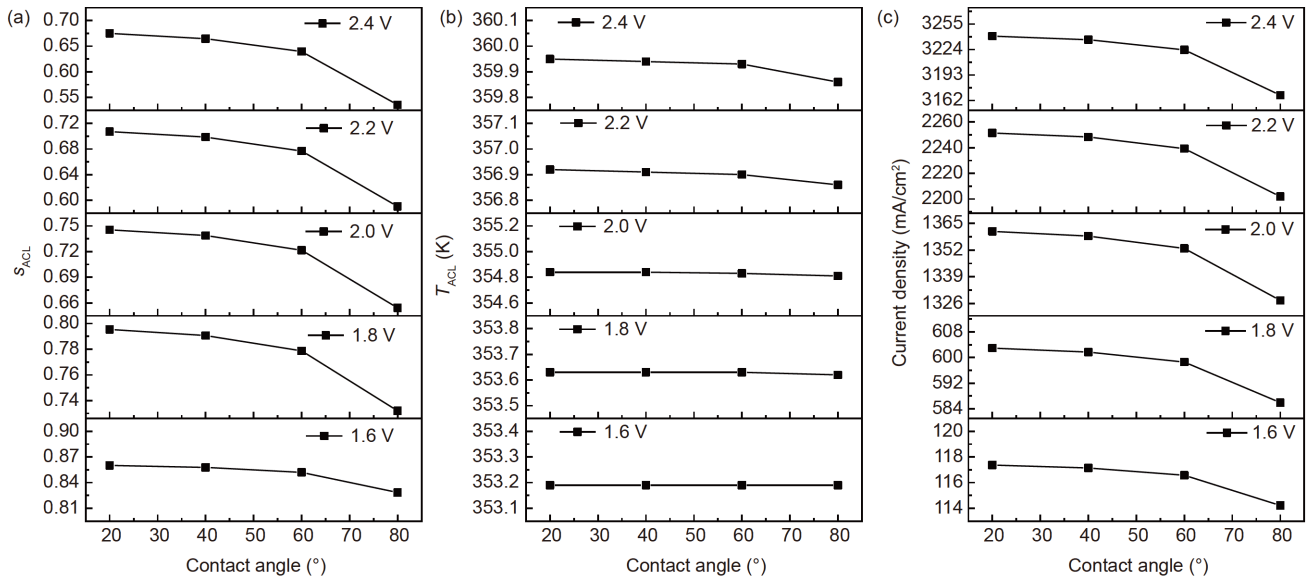
Figure 10   Variations of the liquid saturation in ACL (a), the averaged temperature of ACL (b), and the current density (c) with the contact angle at different voltages.

increase of contact angle, especially when the contact angle changes from 60° to 80°. With the increase of the voltage, the difference of liquid water saturation gets larger. At the voltage of 2.4 V, the liquid water saturation decreases from 0.67 to 0.54 when increasing the contact angle from 20° to 80°. From Figure 10(b), it can be seen that there seems to be no impact on the temperature at low voltage and small contact angle. When the voltage is high, the contact angle shows little impact on the temperature in the ACL, and the maximum change is only 0.09 K at 2.4 V. The results indicate that changing the contact angle has no effect on the temperature. For the current density shown in Figure 10(c), it decreases to some extent with the increase of contact angle, which is consistent with the trend of liquid water saturation in the ACL in Figure 10(a). Therefore, a low contact angle for the AGDL is beneficial for the cell performance because it promotes the water transport through the AGDL.

Figure 11 shows the variations of liquid water saturation, averaged temperature and current density with the AGDL porosity. The AGDL porosity is varied on the range of 0.3 to 0.7 while the contact angle is kept at 80° and the inlet water temperature is 80°C. As can be seen from Figure 11(a), the liquid water saturation increases with the increase of the AGDL porosity. Because high porosity has a positive influence on the gas-liquid transport process, oxygen moves from ACL to ACH more easily. As shown in Figure 11(b), the temperature increases gradually with the increase of porosity and voltage, and the maximum of the temperature difference with the porosity of 0.3 and 0.7 is 0.5 K, which can be negligible compared with the cell temperature. From Figure 11(c), the current density can be increased slightly with the increase of the porosity. However, within the range of tested voltage, the influence of the AGDL porosity on the current density is quite small.

From the above results, it can be concluded that a small contact angle and a high porosity of the AGDL are beneficial to the liquid water and gas transport in a PEMEC, which is consistent with ref. [45].

5 Conclusions

A 3-D heat and two-phase mass transport model for the PEMEC is built in this work. The water and temperature distributions are considered in the model through the coupling calculation of multiple equations, especially the Butler-Volmer equation to which the variables (liquid water saturation and temperature) are added. The distributions of liquid water and temperature with different operating and physical parameters are examined and discussed in detail. The key findings of this study can be summarized as follows.

(1) The liquid water saturation decreases along the y-direction and from the channel to the CL for both the anode and cathode. And the liquid water saturations under the rib are smaller than that facing the channel. The concentration distribution and magnitudes of oxygen and hydrogen have little difference.

(2) There are two apparent temperature gradients along the flow direction and z direction, because of the drop of heat transfer performance, which is caused by the decrease of liquid water saturation and the increase of the fluid temperature. The temperature of each part and the temperature difference present an increase with the increase of voltage. That may cause the overheat at the end of the cell.

(3) Raising the inlet velocity can increase the liquid water saturation and decrease the temperature of the PEMEC. As
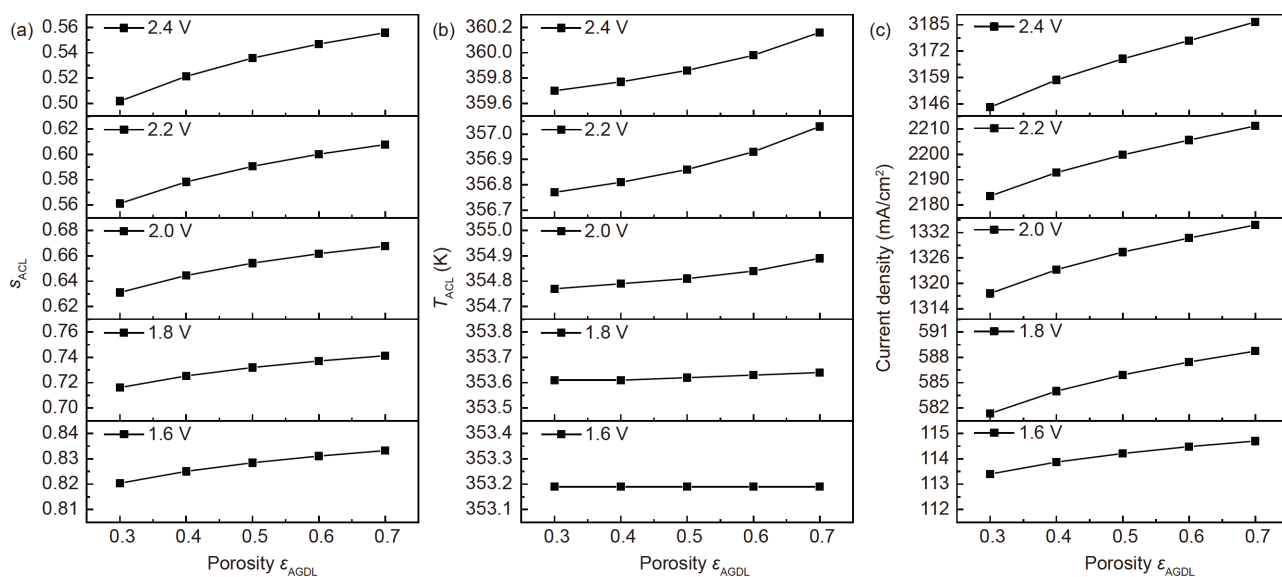
Figure 11 Variations of the liquid saturation in ACL (a), the averaged temperature of ACL (b), and the current density (c) with the porosity at different voltages.

the voltage increases, the priority factor changes from the liquid water saturation increase to the temperature drop in the ACL with the increase of inlet velocity.

(4) A small contact angle and a high porosity of the AGDL are beneficial to the liquid water and gas transport in a PE-MEC. Unlike the negligible effect on the temperature distribution in the ACL, the contact angle and porosity of AGDL can affect the liquid water distribution, and further influence the cell performance.

(5) The effect of various parameters on the PEMEC is of interaction and restricted mutually. For instance, improving the voltage and the inlet temperature can enhance the reaction, but the oxygen bubbles generated in the anode in turn cause more serious loss of mass-transfer polarization, and thus affect the cell performance.

Supporting Information

The supporting information is available online at tech.scichina.com and link.springer.com. The supporting materials are published as submitted, without typesetting or editing. The responsibility for scientific accuracy and content remains entirely with the authors.

1 Dincer I, Acar C. Review and evaluation of hydrogen production methods for better sustainability. Int J Hydrogen Energy, 2015, 40: 11094–11111

2 Hosseini S E, Wahid M A. Hydrogen production from renewable and sustainable energy resources: Promising green energy carrier for clean development. Renew Sustain Energy Rev, 2016, 57: 850–866

3 Baykara S Z. Hydrogen: A brief overview on its sources, production and environmental impact. Int J Hydrogen Energy, 2018, 43: 10605–10614

4 Marshall A, Sunde S, Tsypkin M, et al. Performance of a PEM water electrolysis cell using Ir$_x$Ru$_y$Ta$_z$O$_2$ electrocatalysts for the oxygen evolution electrode. Int J Hydrogen Energy, 2007, 32: 2320–2324

5 Schmidt O, Gambhir A, Staffell I, et al. Future cost and performance of water electrolysis: An expert elicitation study. Int J Hydrogen Energy, 2017, 42: 30470–30492

6 Ito H, Maeda T, Nakano A, et al. Effect of flow regime of circulating water on a proton exchange membrane electrolyzer. Int J Hydrogen Energy, 2010, 35: 9550–9560

7 Ito H, Maeda T, Nakano A, et al. Experimental study on porous current collectors of PEM electrolyzers. Int J Hydrogen Energy, 2012, 37: 7418–7428

8 Dedigama I, Angeli P, van Dijk N, et al. Current density mapping and optical flow visualisation of a polymer electrolyte membrane water electrolyser. J Power Sources, 2014, 265: 97–103

9 Sadeghi Lafmejani S, Olesen A C, Kaer S K. Analysing gas-liquid flow in PEM electrolyser micro-channels. ECS Trans, 2016, 75: 1121–1127

10 Selamet O F, Pasaogullari U, Spernjak D, et al. Two-phase flow in a proton exchange membrane electrolyzer visualized *in situ* by simultaneous neutron radiography and optical imaging. Int J Hydrogen Energy, 2013, 38: 5823–5835

11 Majasan J O, Cho J I S, Dedigama I, et al. Two-phase flow behaviour and performance of polymer electrolyte membrane electrolysers: Electrochemical and optical characterisation. Int J Hydrogen Energy,

12 Lee C, Lee J K, Zhao B, et al. Temperature-dependent gas accumulation in polymer electrolyte membrane electrolyzer porous transport layers. J Power Sources, 2020, 446: 227312

13 Kim H, Park M, Lee K S. One-dimensional dynamic modeling of a high-pressure water electrolysis system for hydrogen production. Int J Hydrogen Energy, 2013, 38: 2596–2609

14 Han B, Mo J, Kang Z, et al. Effects of membrane electrode assembly properties on two-phase transport and performance in proton exchange membrane electrolyzer cells. Electrochim Acta, 2016, 188: 317–326

15 Moradi Nafchi F, Afshari E, Baniasadi E, et al. A parametric study of polymer membrane electrolyser performance, energy and exergy analyses. Int J Hydrogen Energy, 2019, 44: 18662–18670

16 Abdin Z, Webb C J, Gray E M A. Modelling and simulation of a proton exchange membrane (PEM) electrolyser cell. Int J Hydrogen Energy, 2015, 40: 13243–13257

17 Grigoriev S A, Kalinnikov A A, Millet P, et al. Mathematical modeling of high-pressure PEM water electrolysis. J Appl Electrochem, 2010, 40: 921–932

18 Han B, Mo J, Kang Z, et al. Modeling of two-phase transport in proton exchange membrane electrolyzer cells for hydrogen energy. Int J Hydrogen Energy, 2017, 42: 4478–4489

19 Aubras F, Deseure J, Kadjo J J A, et al. Two-dimensional model of low-pressure PEM electrolyser: Two-phase flow regime, electrochemical modelling and experimental validation. Int J Hydrogen Energy, 2017, 42: 26203–26216

20 Kaya M F, Demir N. Numerical investigation of PEM water electrolysis performance for different oxygen evolution electrocatalysts. Fuel Cells, 2017, 17: 37–47

21 Zinser A, Papakonstantinou G, Sundmacher K. Analysis of mass transport processes in the anodic porous transport layer in PEM water electrolysers. Int J Hydrogen Energy, 2019, 44: 28077–28087

22 Nie J, Chen Y, Cohen S, et al. Numerical and experimental study of three-dimensional fluid flow in the bipolar plate of a PEM electrolysis cell. Int J Thermal Sci, 2009, 48: 1914–1922

23 Nie J, Chen Y. Numerical modeling of three-dimensional two-phase gas-liquid flow in the flow field plate of a PEM electrolysis cell. Int J Hydrogen Energy, 2010, 35: 3183–3197

24 De Haro Ruiz D, Sasmito A P, Shamim T. Numerical investigation of the high temperature PEM electrolyzer: Effect of flow channel configurations. ECS Trans, 2013, 58: 99–112

25 Olesen A C, Rømer C, Kær S K. A numerical study of the gas-liquid, two-phase flow maldistribution in the anode of a high pressure PEM water electrolysis cell. Int J Hydrogen Energy, 2016, 41: 52–68

26 Olesen A C, Frensch S H, Kær S K. Towards uniformly distributed heat, mass and charge: A flow field design study for high pressure and high current density operation of PEM electrolysis cells. Electrochim Acta, 2019, 293: 476–495

27 Lafmejani S S, Olesen A C, Kær S K. VOF modelling of gas-liquid flow in PEM water electrolysis cell micro-channels. Int J Hydrogen Energy, 2017, 42: 16333–16344

28 Toghyani S, Afshari E, Baniasadi E, et al. Thermal and electrochemical analysis of different flow field patterns in a PEM electrolyzer. Electrochim Acta, 2018, 267: 234–245

29 Upadhyay M, Lee S, Jung S, et al. Systematic assessment of the anode flow field hydrodynamics in a new circular PEM water electrolyser. Int J Hydrogen Energy, 2020, 45: 20765–20775

30 Zhang Z, Xing X. Simulation and experiment of heat and mass transfer in a proton exchange membrane electrolysis cell. Int J Hydrogen Energy, 2020, 45: 20184–20193

31 Jin D, Ocone R, Jiao K, et al. Energy and AI. Energy AI, 2020, 1: 100002

32 Wang H, Yin Y, Hui X Y, et al. Prediction of effective diffusivity of porous media using deep learning method based on sample structure information self-amplification. Energy AI, 2020, 2: 100035

33 Ferrero D, Santarelli M. Investigation of a novel concept for hydrogen production by PEM water electrolysis integrated with multi-junction

solar cells. Energy Convers Manage, 2017, 148: 16–29

34 Wu H W, Shih G J, Chen Y B. Effect of operational parameters on transport and performance of a PEM fuel cell with the best protrusive gas diffusion layer arrangement. Appl Energy, 2018, 220: 47–58

35 Cao T F, Lin H, Chen L, et al. Numerical investigation of the coupled water and thermal management in PEM fuel cell. Appl Energy, 2013, 112: 1115–1125

36 Sun P. Modeling studies and efficient numerical methods for proton exchange membrane fuel cell. Comput Methods Appl Mech Eng, 2011, 200: 3324–3340

37 Ito H, Maeda T, Nakano A, et al. Properties of Nafion membranes under PEM water electrolysis conditions. Int J Hydrogen Energy, 2011, 36: 10527–10540

38 Chandesris M, Médeau V, Guillet N, et al. Membrane degradation in PEM water electrolyzer: Numerical modeling and experimental evidence of the influence of temperature and current density. Int J Hydrogen Energy, 2015, 40: 1353–1366

39 Xing L, Du S, Chen R, et al. Anode partial flooding modelling of proton exchange membrane fuel cells: Model development and validation. Energy, 2016, 96: 80–95

40 Xu C, Faghri A. Water transport characteristics in a passive liquid-feed DMFC. Int J Heat Mass Transfer, 2010, 53: 1951–1966

41 Guo H, Guo Q, Ye F, et al. Three-dimensional two-phase simulation of a unitized regenerative fuel cell during mode switching from electrolytic cell to fuel cell. Energy Convers Manage, 2019, 195: 989–1003

42 Olivier P, Bourasseau C, Bouamama P B. Low-temperature electrolysis system modelling: A review. Renew Sustain Energy Rev, 2017, 78: 280–300

43 Kaya M F, Demir N, Rees N V, et al. Improving PEM water electrolyser's performance by magnetic field application. Appl Energy, 2020, 264: 114721

44 Babic U, Suermann M, Büchi F N, et al. Critical review—Identifying critical gaps for polymer electrolyte water electrolysis development. J Electrochem Soc, 2017, 164: F387–F399

45 Mo J, Steen S, Zhang F-Y. High-speed and micro-scale measurements of flow and reaction dynamics for sustainable energy storage. In: Proceedings of the 13th International Energy Conversion Engineering Conference. Orlando: American Institute of Aeronautics and Astronautics, 2015